Toward global beyond-mean-field calculations of nuclear masses and low-energy spectra

Tomás R. Rodríguez,[1,2] Alexander Arzhanov,[2] and Gabriel Martínez-Pinedo[2,3]

[1] *Departamento de Física Teórica, Universidad Autónoma de Madrid, E-28049 Madrid, Spain*
[2] *Institut für Kernphysik, Technische Universität Darmstadt, D-64289 Darmstadt, Germany*
[3] *GSI Helmholtzzentrum für Schwerionenforschung, Planckstraße 1, 64291 Darmstadt, Germany*

(Dated: April 21, 2015)

Self-consistent mean field (MF) and beyond-mean-field (BMF) calculations of masses, separation energies and 2_1^+ excitation energies of even-even nuclei where experimental data is available are presented. The functionals used are based on the Gogny D1S and D1M parametrizations and the method includes beyond-mean-field corrections coming from both axial quadrupole shape mixing and symmetry restorations without assuming gaussian overlap approximations. A comparison between mean field, beyond-mean-field approaches and the experimental data is provided. Additionally, the convergence of the results and the possible reduction of the magic shell gaps by including BMF effects are also discussed.

arXiv:1407.7699v3 [nucl-th] 20 Apr 2015

I. INTRODUCTION

Nuclear binding energies are one of the most relevant quantities that define the atomic nucleus. Apart from their intrinsic interest, the nuclear masses are specially important in determining the nucleosynthesis processes that occur in astrophysical environments. For example, they determine the limits of existence of the nucleus as a bound system of protons and neutrons (drip lines), the Q-values for β and α decays, the particle separation energies that are needed to compute capture/emission rates, etc. Therefore, a great effort in measuring masses of very exotic (short-lived) nuclei with high precision is currently made with the use of trapping and/or storage rings techniques [1].

Despite this significant progress, and the one expected in the near future with the arrival of new facilities worldwide, many nuclei will not be experimentally reachable. Particularly important are those belonging to neutron rich regions that are relevant to better constraint the rapid neutron capture (r-process) nucleosynthesis, the mechanism behind the origin of more than the half of the elements beyond iron in the universe. Hence, nuclear models able to compute with high precision the known masses, as well as to provide reliable extrapolations, are very much demanded.

Current theoretical nuclear mass tables are provided mainly by three different approaches: (a) Microscopic-macroscopic (mic-mac) methods which improve the original liquid drop formula with microscopic corrections. The most commonly used of this kind are the finite range droplet model (FRDM) [2, 3] or, more recently, the Weizsäcker-Skyrme (WS) mass model [4, 5]. (b) Duflo-Zuker (DZ) approach based a functional of occupation numbers guided by the interacting shell model method [6]. (c) Microscopic methods based on Hartree-Fock-Bogoliubov (HFB) approaches with Skyrme (see Ref. [7, 8] and references therein) and Gogny functionals [9]. The above methods have reached a root mean square (RMS) deviation from data [10, 11] of 0.57 MeV (FRDM), 0.298 MeV (WS), 0.36 MeV (DZ), 0.51 MeV (HFB-Skyrme) and 0.798 MeV (HFB-Gogny).

This impressive agreement to the global behavior of the known masses is not sufficient to have a full confidence in the extrapolations to unknown regions since large deviations in the predictions of the different models are found. In addition, even if the overall performance is similar, some local deviations between the models in sensitive regions can largely affect the results of nucleosynthesis simulations [12, 13]. Therefore, theoretical models should be improved to reduce such uncertainties. In particular, *ab-initio* calculations are becoming available for medium mass systems although currently neither the range of applicability nor the accuracy reached by such methods are good enough to be applied to astrophysical purposes [14–20]. Hence, in the short-mid term energy density functionals are still the most promising microscopic methods to compute nuclear properties in the whole nuclear chart with the required accuracy. These methods have been improved significantly in the last years by taking into account not only global fits to all known masses but also some constraints coming from *ab-initio* calculations in infinite nuclear matter [7, 21, 22].

However, a mean field (HFB) approach is commonly used to solve the nuclear many-body problem and beyond-mean-field (BMF) corrections have been included phenomenologically to mimic rotational and vibrational corrections [23]. Nevertheless, in the last decade, a better treatment of such BMF correlations of even-even nuclei using symmetry restorations and configuration mixing methods have been implemented with Skyrme, Relativistic and Gogny interactions [24]. These improvements have allowed the study of the appearance/disappearance of shell closures or shape mixing/coexistence/transitions phenomena, for example. Concerning nuclear masses, these BMF correlations have been computed globally using particle number and angular momentum projection and generator coordinate method (GCM) with Skyrme interactions [25, 26] and using the five dimensional collective hamiltonian (5DCH) with Gogny [9, 27] and, more recently, Relativistic [28] interactions. Due to the large

computational burden of performing GCM with particle number and angular momentum restorations, these pioneer global surveys were carried out assuming gaussian overlap approximations (GOA).

In this paper we present the results of global calculations for even-even nuclei performed with the Gogny D1S [29, 30] and D1M [9] interactions using implementations of the GCM and quantum number projection methods without gaussian overlap approximations. Additionally, we discuss the convergence of the results -both HFB and BMF- as a function of the number of oscillator shells included in the basis where the many-body wave functions are expanded.

Results for odd systems including such advanced many-body techniques are still not available with the Gogny interaction although some preliminary calculations in a single nucleus have been recently reported with Skyrme forces [31]. Additionally, in this survey we assume axial and parity symmetry conserving intrinsic states, exploring explicitly the axial quadrupole degree of freedom by performing one-dimensional GCM calculations. Including triaxiality and/or octupolarity within the present framework increases prohibitively the computational time and it is beyond the scope of the present study. Nevertheless, global calculations including the triaxial [9, 27, 32], and octupole [33, 34] degrees of freedom within less involved many-body methods have been reported. In particular, 159 out of 5900 nuclei with triaxial ground states are found in the FRDM model [32]. The largest differences in binding energies, $\lesssim 0.6$ MeV, are obtained in regions around ^{108}Ru and ^{140}Gd. In Ref. [27] most of the nuclei are predicted to be axial symmetric (spherical, prolate and oblate) at the HFB level with Gogny D1S. BMF correlations within the 5DCH bring all the nuclei toward triaxial shapes –in average– even though in the HFB approximation are predicted spherical and/or axial symmetric. On the other hand, following Ref. [34], only a few out of 818 nuclei calculated with Gogny D1S-D1N-D1M between $8 \leq Z \leq 110$ are octupole deformed in the HFB ground state. These nuclei are obtained around Ra, Ba and Zr region and the energy gain with respect to the octupole symmetric states are $\lesssim 1.2$ MeV. Further BMF correlations including parity projection and GCM along the β_3 degree of freedom give extra binding energies as large as 2.5 MeV in the regions showing octupole deformation at the HFB level. However, in the rest of nuclei these correlation energies are of the order of 1 MeV and vary smoothly with N and Z, producing an almost constant shift in the total energies.

This document is organized as follows: First, a description of the method used to compute masses is given in Sec. II. Then, the results are discussed in Sec. III. Finally, a brief summary and outlook are presented in Sec. IV.

II. THEORETICAL FRAMEWORK

The total energy (negative in our convention) of a given nucleus is calculated in the present work as the sum of two terms:

$$E = E_{\rm HFB} + \Delta E_{\rm BMF} \tag{1}$$

where $E_{\rm HFB}$ is the Hartree-Fock-Bogoliubov (HFB) energy (mean field) and $\Delta E_{\rm BMF}$ is a beyond-mean-field (BMF) correction which includes particle number restoration, angular momentum projection and axial quadrupole shape mixing within the generator coordinate method (GCM) [35]. Both terms are computed with the same underlying interaction, namely, Gogny D1S or D1M parametrization.

For the sake of simplifying the notation, we express the theoretical energy throughout this work as the expectation value of a hamiltonian operator. However, it is important to point out that since the effective interactions used here are density-dependent, this notation is not truly rigorous and energy density functionals (EDFs) should be defined instead of such expectation values. We refer to Ref. [36] for a general discussion about this topic and Refs. [37, 38] for the particular choice of the corresponding EDFs used in this work.

A. Mean field (HFB) approach

We start by reviewing briefly the HFB method [35]. In this microscopic approach, based on the variational principle, the many-body wave function of the atomic nucleus is searched among a set of trial wave functions that are defined as quasiparticle vacua, $|\phi\rangle$:

$$\hat{\beta}_k|\phi\rangle = 0 \;\forall\; k \tag{2}$$

Those quasiparticles are defined as the most general linear combination of creation ($\hat{c}_l^\dagger$) and annihilation ($\hat{c}_l$) single particle operators:

$$\hat{\beta}_k^\dagger = \sum_l U_{lk}\hat{c}_l^\dagger + V_{lk}\hat{c}_l, \tag{3}$$

where U, and V are the variational parameters. Since Eq. 3 breaks most of the symmetries of the original interaction, in particular, the particle number symmetry, the HFB wave function is constrained to have the correct mean value of the number of particles. Therefore, the HFB equations [35] are found by the condition:

$$\delta\left(E'_{\rm HFB}\left[|\phi\rangle\right]\right)_{|\phi\rangle=|{\rm HFB}\rangle} = 0 \tag{4}$$

with

$$E'_{\rm HFB}\left[|\phi\rangle\right] = \langle\phi|\hat{H}|\phi\rangle - \lambda_N\langle\phi|\hat{N}|\phi\rangle - \lambda_Z\langle\phi|\hat{Z}|\phi\rangle, \tag{5}$$

where $\hat{H}$, $\hat{N}(\hat{Z})$ are the hamiltonian and the neutron (proton) number operators, respectively; $|\phi\rangle = |\mathrm{HFB}\rangle$ is the HFB solution obtained by solving the corresponding HFB equations (Eqs. 4-5); and $\lambda_{N(Z)}$ is a Lagrange multiplier which ensures $\langle\phi|\hat{N}(\hat{Z})|\phi\rangle = N(Z)$. The normalization $\langle\phi|\phi\rangle = 1$ is also assumed.

In practical applications, the spherical harmonic oscillator (s.h.o.) basis is usually chosen as the working basis where the quasiparticles defined in Eq. 3 are expanded [39]. The sum in such an equation runs over an infinite number of s.h.o. states but this sum must be truncated in actual implementations in computer codes. The results should not depend on the choice of the basis and the convergence of the results are obtained if a sufficiently large number of major s.h.o. shells ($N_{s.h.o.}$) are included. However, the computational burden increases significantly with the number of oscillator shells and a compromise between a better convergence and a reasonable computational time has to be considered (see discussion below). In the present work, $E_{\mathrm{HFB}} = \langle\mathrm{HFB}|\hat{H}|\mathrm{HFB}\rangle$ in Eq. 1 is computed with $N_{s.h.o.} = 19$.

B. Beyond-mean-field (BMF) approach

The second term in the energy (ΔE_{BMF} in Eq. 1) corresponds to corrections beyond the mean field (HFB) approximation. In principle, the energy should be computed by using BMF methods from the first place. However, these methods are much more time consuming than the corresponding HFB and the size of the s.h.o. basis used in this case is generally smaller. In the present work, $N_{s.h.o.} = 11$ has been chosen for computing BMF effects. Hence, BMF correction is defined as:

$$\Delta E_{\mathrm{BMF}} = E_{\mathrm{BMF}}(N_{s.h.o.} = 11) - E_{\mathrm{HFB}}(N_{s.h.o.} = 11) \quad (6)$$

This energy difference is less dependent on the number of oscillator shells included in the basis than the total energies separately, E_{HFB} and E_{BMF}. We will study explicitly this point below.

In the above equation, $E_{\mathrm{BMF}}(N_{s.h.o.} = 11)$ is computed within a symmetry conserving configuration mixing (SCCM) framework. The method contains simultaneous particle number and angular momentum projection (PNAMP) of different intrinsic Hartree-Fock-Bogoliubov-type states and a subsequent mixing of these states performed within the generator coordinate method (GCM) framework. In general, different shapes (axial and non-axial) and collective coordinates can be included in the GCM calculation. However, the addition of more generating coordinates largely increases the computational time, especially if a triaxial angular momentum projection is performed. Therefore, we have focused on the mixing of axial deformed and parity conserving states. Further extensions will be explored in a future study. Nevertheless, contrary to other BMF approaches like the 5DCH, this method is variationally consistent with the underlying HFB functional, i.e., lower total energies are always obtained when such correlations are taken into account. Furthermore, the more collective coordinates and symmetry restorations are included in the GCM the lower is the ground state energy obtained until the exact solution is eventually obtained. In this sense, the method is extensible to other degrees of freedom (triaxiality, octupolarity, pairing content, ...) without loosing its variational character. Finally, although the present calculations are restricted to axial, parity and time-reversal symmetric intrinsic states, the method can be applied to the whole nuclear chart. If a specific nucleus turns out to be, for instance, triaxial and/or octupole deformed, the amount of correlations obtained here will be smaller, though neither negligible nor meaningless, than the ones eventually obtained with including those degrees of freedom.

In the following, the particular realization of the SCCM method used here is described step-by-step.

1. *Variation after particle number projection method (PN-VAP)*

In contrast to the previous section (Sec. II A), the particle number projected energy is minimized instead of the HFB one. This is the so-called variation after particle number projection (PN-VAP) [35, 40]. Furthermore, the set of intrinsic, HFB-type, trial wave functions, $|\phi(\beta_2)\rangle$, are also constrained to have a given value of the axial quadrupole deformation, β_2. Hence, the variational equation now reads as:

$$\delta\left(E'_{\mathrm{PN-VAP}}\left[|\phi\rangle\right]\right)_{|\phi\rangle=|\mathrm{PNVAP}\rangle} = 0, \quad (7)$$

with $|\phi(\beta_2)\rangle = |\mathrm{PNVAP}(\beta_2)\rangle$ is the intrinsic wave function that minimizes the functional:

$$E'_{\mathrm{PN-VAP}}\left[|\phi\rangle\right] = \frac{\langle\phi|\hat{H}P^N P^Z|\phi\rangle}{\langle\phi|P^N P^Z|\phi\rangle} - \lambda_{q_{20}}\langle\phi|\hat{Q}_{20}|\phi\rangle. \quad (8)$$

Here, $P^{N(Z)}$ is the projector onto good number of neutrons (protons) [35],$\hat{Q}_{20} = r^2 Y_{20}(\theta,\varphi)$ is the axial quadrupole operator and the Lagrange multiplier $\lambda_{q_{20}}$ ensures the condition: $\lambda_{q_{20}} \rightarrow \langle\phi|\hat{Q}_{20}|\phi\rangle = q_{20}$. The quadrupole deformation parameter β_2 is related to q_{20} by:

$$q_{20} = \pm\frac{\beta_2}{C}; \quad C = \sqrt{\frac{5}{4\pi}}\frac{4\pi}{3r_0^2 A^{5/3}} \quad (9)$$

being $r_0 = 1.2$ fm, A the mass number and the plus (minus) sign indicates prolate (oblate) shapes. Hence, the collective intrinsic deformation is well established within this framework and this fact allows the description of the states in the laboratory frame in terms of their intrinsic shapes unambiguously.

2. Symmetry conserving configuration mixing (SCCM) method

Once the set of intrinsic wave functions -$|\mathrm{PNVAP}(\beta_2)\rangle$- is obtained, the final states are built through the Ansatz provided by the generator coordinate method (GCM) [35]. In this framework, the states are assumed to be linear combinations of particle number and angular momentum projected PN-VAP states:

$$|\Psi^{I\sigma}\rangle = \sum_{\beta_2} g^{I\sigma}_{\beta_2} P^I_{00} P^N P^Z |\mathrm{PNVAP}(\beta_2)\rangle \qquad (10)$$

where I is the total angular momentum, $P^I_{KK'}$ the angular momentum projector applied to axial symmetric intrinsic states ($K = K' = 0$) [35] and σ labels different states obtained for a given value of I. The parameters $g^{I\sigma}_{\beta_2}$ are determined by the Ritz variational principle which leads to the Hill-Wheeler-Griffin (HWG) equation:

$$\delta\left(E^{I\sigma}_{\mathrm{SCCM}}\left[g^{I\sigma}_{\beta_2}\right]\right) = 0 \Rightarrow \sum_{\beta_2'}\left(\mathcal{H}^I_{\beta_2,\beta_2'} - E^{I\sigma}_{\mathrm{SCCM}}\mathcal{N}^I_{\beta_2,\beta_2'}\right) g^{I\sigma}_{\beta_2'} = 0 \qquad (11)$$

The energy and norm overlap matrices are defined as:

$$\begin{aligned}\mathcal{H}^I_{\beta_2,\beta_2'} &= \langle \mathrm{PNVAP}(\beta_2)|\hat{H} P^I_{00} P^N P^Z|\mathrm{PNVAP}(\beta_2')\rangle \\ \mathcal{N}^I_{\beta_2,\beta_2'} &= \langle \mathrm{PNVAP}(\beta_2)|P^I_{00} P^N P^Z|\mathrm{PNVAP}(\beta_2')\rangle\end{aligned} \qquad (12)$$

The resulting HWG equations -one for each value of the angular momentum- provide the energy levels $E^{I\sigma}_{\mathrm{SCCM}}$ and collective wave functions defined in the (β_2) direction.

Hence, the energy including symmetry restorations and shape mixing within this framework is given by:

$$E_{\mathrm{BMF}}(N_{s.h.o.} = 11) = E^{I=0\sigma=1}_{\mathrm{SCCM}} \qquad (13)$$

Obviously, excited states, in particular $E(2^+_1) = E^{I=2\sigma=1}_{\mathrm{SCCM}} - E^{I=0\sigma=1}_{\mathrm{SCCM}}$ excitation energies, can be also calculated within the same framework.

C. Numerical details and convergence of the method

We summarize some details about the actual global calculations. First of all, the HFB [41], PN-VAP [40] and SCCM [42] codes used throughout this work have been developed in the Nuclear Physics Group at the Universidad Autónoma de Madrid. The calculations were performed both in GSI-Prometheus (Darmstadt) [43] and CSC-Loewe (Frankfurt) [44] computing facilities, using scripts optimized to perform such a large scale survey. The HFB (mean field) solutions have been found by using a spherical harmonic oscillator basis with $N_{s.h.o.} = 19$ shells and an optimized oscillator length for each nucleus [45]. Additionally, with this large number of s.h.o. shells, potential energy surfaces along the axial quadrupole degree of freedom were explored to make sure that the unconstrained HFB-calculations did not converge to local meta-stable minima. All terms (direct, exchange and pairing) in the interaction (including Coulomb) have been included here and also in the BMF part. For the GCM part, a set of 15-20 intrinsic many-body wave functions with different axial quadrupole shapes (oblate and prolate) has been found by using the PN-VAP method described above. These

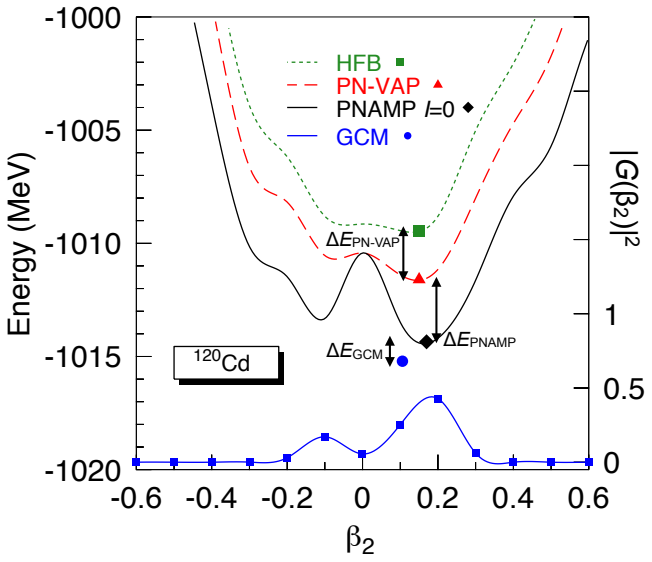

FIG. 1. (color online) Potential energy surfaces as a function of the axial quadrupole deformation calculated with HFB (green dotted line), PN-VAP (red dashed line) and PNAMP (thin black continuous line) approximations for ^{120}Cd with the Gogny D1S parametrization. The square, triangle and diamond represent the minima of each surface respectively. The blue dot corresponds to the full SCCM energy and the blue boxes (connected by a continuous line to guide the eye) represent the ground state collective wave function normalize to 1 ($\sum_{\beta_2} |G(\beta_2)|^2 = 1$). The arrows point out the energy gain between the different approaches considered in this work.

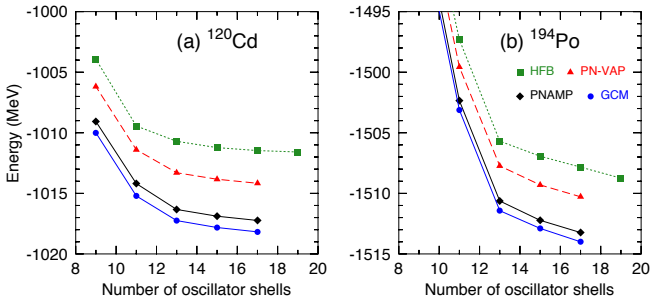

FIG. 2. (color online) Convergence of the energy as a function of the number of major oscillator shells included in the working basis for the same approaches of Fig. 1. Left and right panels correspond to ^{120}Cd and ^{194}Po respectively, calculated with Gogny D1S.

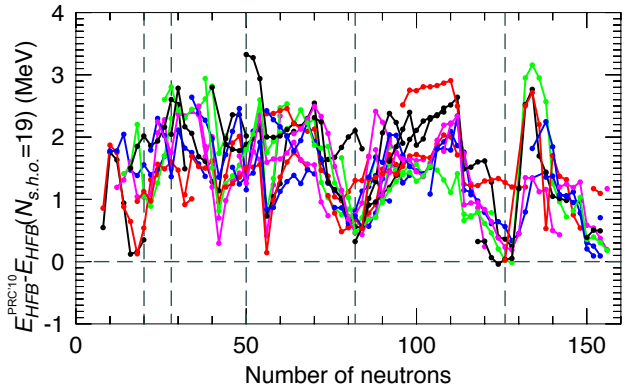

FIG. 3. (color online) Differences between the HFB total energies given in Ref. [27] and the present HFB calculation performed with $N_{s.h.o.} = 19$ and optimized oscillator length. Isotopic chains are connected by lines with the same color and the interaction in all of the cases is Gogny D1S. Positive values mean lower total energies obtained with the present calculation with respect to Ref. [27].

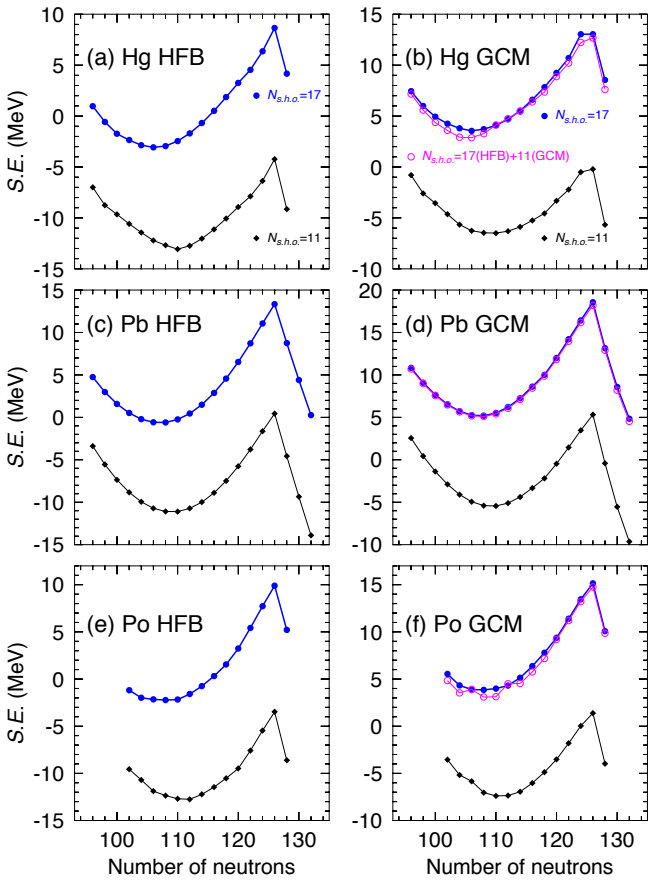

FIG. 4. (color online) Shell effects (Eq. 14) calculated with the HFB (left panel) and GCM (right panel) methods for Hg (top), Pb (middle) and Po (bottom) isotopic chains. Black diamonds and blue dots are calculated with $N_{s.h.o.} = 11$ and 17 respectively. Magenta circles are calculated by adding the BMF corrections computed with $N_{s.h.o.} = 11$ to the HFB result with $N_{s.h.o.} = 17$. All nuclei are computed with the Gogny D1S parametrization.

intrinsic wave functions are expanded in a basis with $N_{s.h.o.} = 11$ shells, again with an optimized oscillator length for each nucleus. The standard number of points used in the integrals in the gauge (particle number projection) and Euler (angular momentum projection) angles were 9 and 16 respectively and the convergence of the quantum number projections were checked by inspecting the mean values of the operators, $\hat{N}$, $\hat{Z}$, $\Delta\hat{N}^2$, $\Delta\hat{Z}^2$ and $\hat{J}^2$.

Finally, the convergence of the solutions of the HWG equations has been ensured by analyzing the energy plateaus as a function of the natural states which transform the HWG equations into regular eigenvalue problems. Detailed expressions and performance of this approach can be found in Refs. [38, 42] (and references therein).

To shed light on how the BMF method used here actually works, the nucleus ^{120}Cd is taken as an example. The HFB –Gogny D1S– energy calculated with $N_{s.h.o.} = 19$ is $E_{\rm HFB} = -1011.786$ MeV. On top of this value, BMF corrections are made (see Eq. 1). As it is mentioned in the previous section, these corrections are performed with $N_{s.h.o.} = 11$. In Fig. 1 the energy as a function of the axial quadrupole deformation β_2 is represented for mean field (HFB, dotted line), variation after particle number projection (PN-VAP, dashed line) and particle number and angular momentum $I = 0$ projection (PNAMP, $I = 0$, thin continuous line) approximations. The minima of each potential energy surfaces are the corresponding energies for each level of approximation (square, HFB; triangle PN-VAP; and diamond PNAMP, $I = 0$). In this case, the value of deformation of all the minima is quite similar ($\beta_2 \sim 0.17$), i.e., ^{120}Cd is prolate deformed in all of these approaches. A gain in the energy (1.96 MeV) is observed when correlations associated to

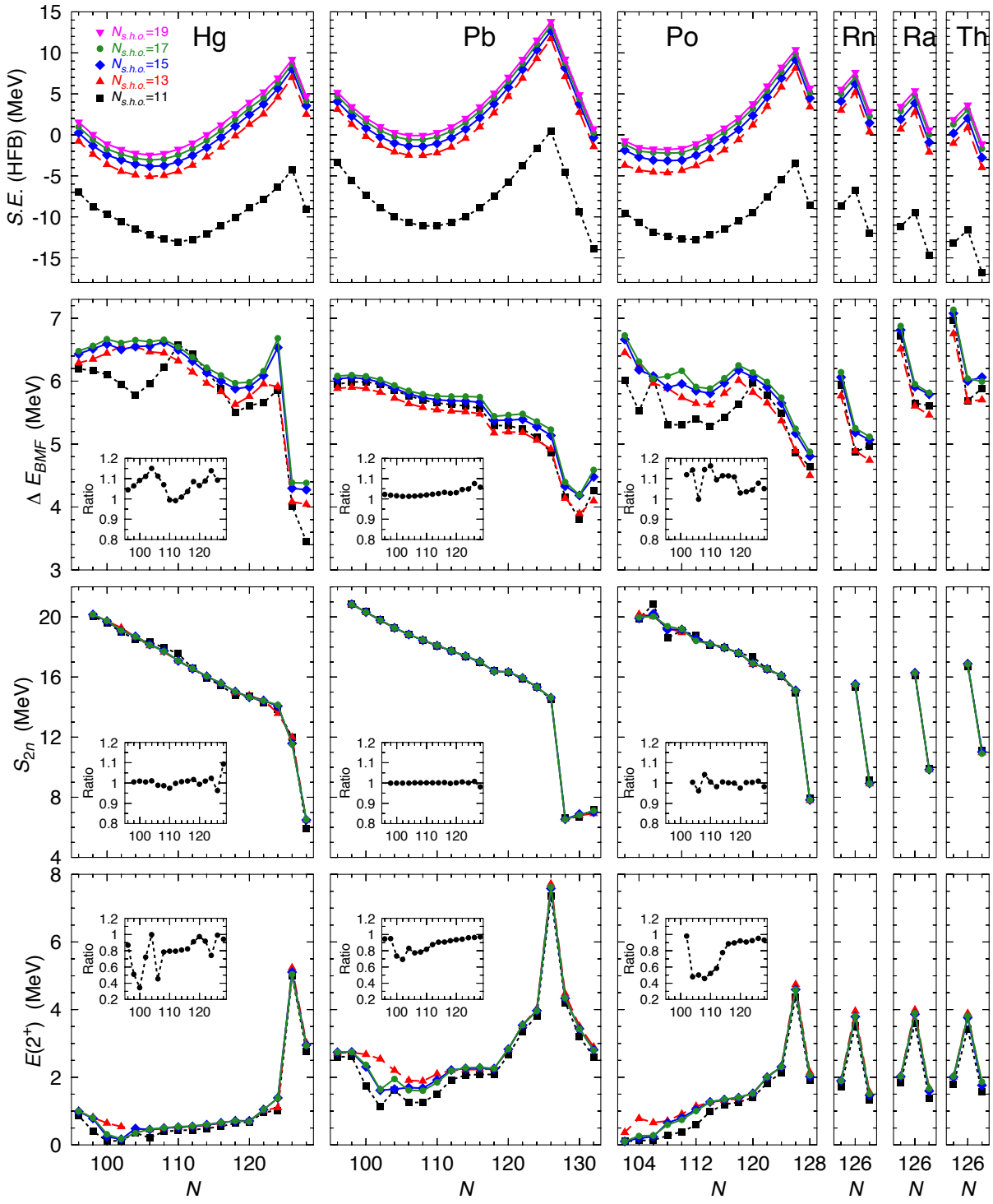

FIG. 5. (color online) Results of the calculations performed with different values of $N_{s.h.o.}$ for Hg, Pb, Po, Rn, Ra and Th isotopes (from left to right). Top panel: Shell effects calculated with the HFB method ; top-middle panel: BMF corrections; bottom-middle panel: two-neutron separation energies with BMF corrections; and bottom panel: 2_1^+ excitation energies. In the insets, the ratios between the results with $N_{s.h.o.} = 17$ and 11 are represented. All nuclei are computed with the Gogny D1S parametrization.

the restoration of the particle number are taken into account. Further correlation energy (2.80 MeV) is obtained when simultaneous particle number and angular momentum projection is performed. In addition, by allowing shape mixing of particle number and angular momentum restored axial states (GCM), Eqs. 10-11, the energy marked by a blue dot in Fig. 1 is obtained, i.e., 1.02 MeV extra energy with respect to the PNAMP ($I = 0$) minimum. The square of so-called ground state collective wave function ($|G(\beta_2)|^2$) is plotted and it represents the probability of having a given β_2 deformation in this state (blue boxes in Fig. 1). In this case, two maxima are found at $\beta_2 \sim -0.1$ and $+0.2$, being the prolate one the absolute maximum. The position of the blue dot in the abscissa axis corresponds to the mean deformation calculated with the ground state collective wave function $\bar{\beta}_2 = 0.10$. In summary, the total correction provided by the current SCCM method is $\Delta E_{\rm BMF} = 5.77$ MeV and the total energy (Eq. 1) is $E(^{120}{\rm Cd}) = -1017.559$ MeV.

We discuss next the performance and convergence of the results as a function of the number of spherical harmonic oscillator shells, $N_{s.h.o.}$, included in the working basis. Since the results should not depend on the size of such a basis if a sufficient large number of single particle states are included, in the ideal situation one should take a very large number for $N_{s.h.o.}$. However, this number is limited by the present computational resources. Thus, the average computing time required at each step of the calculation of one nucleus in a single core, depending on $N_{s.h.o.}$, is shown in Table I. Here, we observe the huge differences in the computational burden between the different approaches, in particular when we compare the values needed for HFB and BMF methods. It is important to point out that while the running time for the GCM part can be established beforehand once the number of shells and GCM points are chosen, for the HFB part, and more critically, for the PN-VAP, those numbers can vary from nucleus to nucleus depending on the rate of convergence of the minimization process (Eqs. 4 and 7). Therefore, the values in Table I refer to average numbers in those cases. We can directly check in Table I that enlarging the number of shells for BMF calculations would increase prohibitively the computational time. In fact, we have chosen $N_{s.h.o.} = 17$ as our current limit for BMF calculations.

$N_{s.h.o.}$	HFB	PN-VAP	GCM
11	∼0.07 h	∼**45 h**	**14.5 h**
13	∼0.20 h	∼120 h	54.4 h
15	∼0.52 h	∼300 h	169.1 h
17	∼0.97 h	∼500 h	460.3 h
19	∼**2.46 h**	–	–

TABLE I. Estimation of the computational time used to calculate one nucleus in one single core at the GSI-Prometheus cluster for each level of approximation described in Sec.II. In boldface, the number of shells chosen in global calculations.

In Fig. 2 we represent the dependence of the total energy, calculated with the different approaches, on the number of oscillator shells for a medium mass nucleus (^{120}Cd mentioned above) and a heavy one (^{194}Po). In both cases we observe an energy gain when increasing $N_{s.h.o.}$ but only for ^{120}Cd a convergence regime is reached for the HFB result (Fig. 2(a)). For the heavy nucleus ^{194}Po (Fig. 2(b)), further energy gain is expected if more single particle states are added to the working basis and $N_{s.h.o.} = 19$ is not a converged value. Therefore, extrapolation methods to an infinite basis should be applied to further converge the total energy [9, 46–51]. The performance and reliability of those extrapolation schemes within the present theoretical framework is a work in progress [52] and we have taken the value with $N_{s.h.o.} = 19$ as our best converged one for the HFB result.

As a matter of fact, in Refs. [27, 47] the HFB energy for Gogny D1S has been computed choosing a number of single particle states equal to eight times the larger number among the protons and neutrons in the nucleus. We have checked this prescription by comparing the Gogny-D1S-HFB values given in the supplemental material of Ref. [27] with our $N_{s.h.o.} = 19$, finding a systematic better convergence in our case of roughly 1.5 MeV in the whole nuclear chart (see Fig. 3). These results point out that convergence of the total energy by using harmonic oscillator bases will be a possible source of problems of the present work which is also shared by previous calculations.

On the other hand, the total energies obtained with PN-VAP, PNAMP and GCM approaches as a function of $N_{s.h.o.}$ are almost parallel to each other, showing that the BMF correlations, $\Delta E_{\rm BMF}$, are less dependent on the number of single particle states included in the basis (Fig. 2). Furthermore, as a consequence of the variational nature of our BMF correlations, larger correlations are obtained with the GCM method than the ones given by PNAMP, being the latter larger than PN-VAP as well.

As it is mentioned above, using Eq. 1 to compute the total energy emerges from the present limitations both in terms of convergence and in computational time. Let us check whether the total energy computed with the SCCM method with a large number of harmonic oscillator shells -$N_{s.h.o.} = 17$ is our limit- can be reproduced with the Eq. 1, computing the HFB part with such a large number of $N_{s.h.o.}$ and $\Delta E_{\rm BMF}$ with the significantly less time consuming $N_{s.h.o.} = 11$ value.

In Figure 4 we show the shell effects computed both with HFB and GCM methods for $Z = 80$, 82 and 84 isotopic chains. Shell effects are defined as the difference between the total (experimental or theoretical) energy and the energy provided by a liquid drop formula (E_{LD}) and it is a convenient way to rescale the total energy:

$$S.E.(Z,N) = E_{LD}(Z,N) - E(Z,N) \qquad (14)$$

We observe first a large difference (up to $\sim$ 10 MeV)

between the shell effects calculated with 11 and 17 oscillator shells within the same many-body approach, HFB or GCM, for all isotopic chains. This shows again explicitly that the total energy calculated with $N_{s.h.o.} = 11$ is not well converged, now in three different isotopic chains. However, we can approach the BMF results with $N_{s.h.o.} = 17$ by adding to the HFB values computed with the same number of oscillator shells, the BMF corrections obtained with $N_{s.h.o.} = 11$. Such a result is represented with magenta circles in Figs. 4(b)-(d)-(f), showing a nice agreement with the GCM values calculated the largest value of $N_{s.h.o.}$ that we can reach for this approach.

Once we have checked the suitability of splitting the total energy in a MF part plus BMF corrections, we have performed additional tests of the convergence of the results in heavy nuclei. Hence, $Z = 80 - 84$ isotopic chains and $N = 124 - 128$ isotonic chains have been calculated in all of the approaches with increasing values of the oscillator shells (with the Gogny D1S parametrization). The results are summarized in Fig. 5 where shell effects (top panel), beyond mean field corrections (top-middle panel), two-neutron separation energies (bottom-middle panel) and 2^+ excitation energies (bottom panel) are shown. In the top panel of Fig. 5 the shell effects corresponding to HFB calculations are represented, although similar patterns but shifted to larger values are found in PN-VAP and GCM results (see right panel of Fig. 4). We observe that increasing $N_{s.h.o.}$ the results tend to collapse to a final curve. However, the differences between the HFB results for $N_{s.h.o.} = 19$ and 17 are around ~ 0.8 MeV in average and one should go to larger number of oscillator shells to get full convergence.

The large differences found in the shell effects for the $N_{s.h.o.} = 11$ and $N_{s.h.o.} = 19$ results (up to 14 MeV) are much smaller in the calculated BMF corrections. Furthermore, they are almost negligible in the two-neutron(proton) separation energies -defined in Eq. 15. However, we also observe some local deviations from the $N_{s.h.o.} = 17$ - chosen to be the best values for BMF approaches- in the neutron deficient Hg, Pb and Po isotopes. In this region, several deformed configurations are almost degenerated (see Ref. [53] and references therein) that can be favored differently depending on the number of oscillator shells. Hence, those small jumps are produced by a change in deformation. In any case, the largest difference are around 0.9 MeV but still could lead to small artificial jumps in $S_{2n(2p)}$ and/or $E(2_1^+)$. The above aspects are also visualized in the corresponding ratios between the results with $N_{s.h.o.} = 17$ and $N_{s.h.o.} = 11$ represented in the insets of Fig. 5. Therefore, these convergence effects should be taken into account for improving the precision of the mass models.

Finally, the comparison with the available experimental data for even-even nuclei requires the calculation of 598 nuclei for each parametrization of the Gogny functional, i.e., 1196 nuclei. Therefore, as it was mentioned in previous sections, the present global survey has been restricted to compute the HFB energy and the beyond-mean-field corrections using $N_{s.h.o.} = 19$ and 11 respectively. According to the previous analysis, this choice seems to be a reasonable compromise between convergence and computational time. This means that the calculation of one nucleus within the prescription followed in this work takes ~ 62 hours/core at the GSI-Prometheus cluster, which is still feasible with our current facilities.

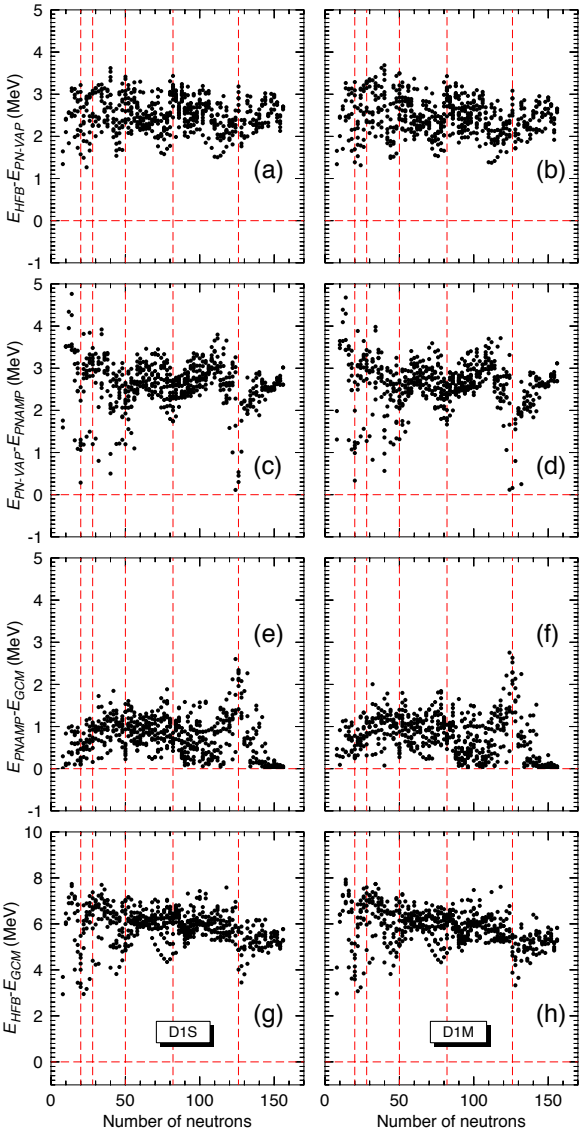

FIG. 6. (color online) Gain in total energy as a function of the number of neutrons obtained by including (a)-(b) variation after particle number projection (PN-VAP) method; (c)-(d) Simultaneous particle number and angular momentum $I = 0$ projection (PNAMP); (e)-(f) quadrupole shape mixing within the generator coordinate method (GCM) with symmetry restored states; and (g)-(h) total beyond-mean-field gain. Dashed vertical lines represent the neutron magic numbers 20, 28, 50, 82 and 126. Left and right panels correspond to Gogny D1S and D1M parametrizations, respectively.

III. RESULTS

A. BMF correlation energies

We now generalize the results obtained in Fig. 1 to the even-even nuclei with $Z, N \geq 10$ contained in the most recent Atomic Mass Evaluation (AME) [11] both for Gogny D1S and D1M parametrizations. In Fig. 6 the successive gains in total energy reached by restoring the symmetries and allowing the axial quadrupole shape mixing are represented as a function of the number of neutrons. The first noticeable aspect is the striking similarity between those correlation energies for both D1S and D1M parametrizations. We observe a band of values ranged in the interval 1.5–3.5 MeV with a mean gain ~ 2.3 MeV of correlation energy with respect to the mean field (HFB) solutions when variation after particle number projection (PN-VAP) method is applied (Figs. 6(a)-(b)). In addition, some local minima are obtained around $\sim 24, \sim 44, \sim 78$ and ~ 110, right before the neutron magic numbers 28, 50, 82 and 126 for both D1S and D1M parametrizations.

Minima are also found both in the energy gained by particle number and angular momentum restoration (PNAMP) -on top of PN-VAP- and by the generator coordinate method (GCM) -on top of PNAMP- but now located at the shell closures. In the former (Figs. 6(c)-(d)), larger correlation energies are obtained in the mid-shell and minima are found at the neutron magic numbers. Excluding the lighter and the semi-magic nuclei, an average gain of ~ 2.7 MeV is attained and a slightly decreasing slope is also observed when increasing the number of neutrons. Concerning the GCM correlation energies (Figs. 6(e)-(f)), contrary to PNAMP, the larger gains are almost at the shell closures, obtaining a clear maximum at $N = 126$. The average gain in this case is ~ 0.8 MeV. This behavior of the BMF energies is important to correct the parabolic shape observed in experimental theoretical energy differences at the HFB level (see fig. 10).

Finally, the total beyond-mean-field energy gain (summing up all of the previous contributions) is represented in Figs. 6(g)-(h). We observe first that smaller correlation energies are obtained around the magic numbers, producing qualitatively an inverted parabolic behavior between two consecutive shell closures. Furthermore, we see a larger spread in the BMF energy gain in the lighter nuclei. Finally, the overall gain is slightly smaller when the number of neutrons is increased for both parametrizations.

Analogous patterns as the ones just described above are found for the different levels of approximation when they are represented as a function of the number of protons (see Fig. 7). Hence, a rather flat energy gain for the PN-VAP approach is obtained both for D1S and D1M parametrizations (Figs. 7(a)-(b)). Furthermore, the local minima are found now at the proton magic numbers 20, 28, 50 and 82 in this approximation. For PNAMP (Figs. 7(c)-(d)) and GCM (Figs. 7(e)-(f)) approaches we do not observe differences either between the parametrizations. In the former, shell effects are still present at $Z = 20$, 28, 40 and 82; in the latter, the lead isotopes have the most prominent ones.

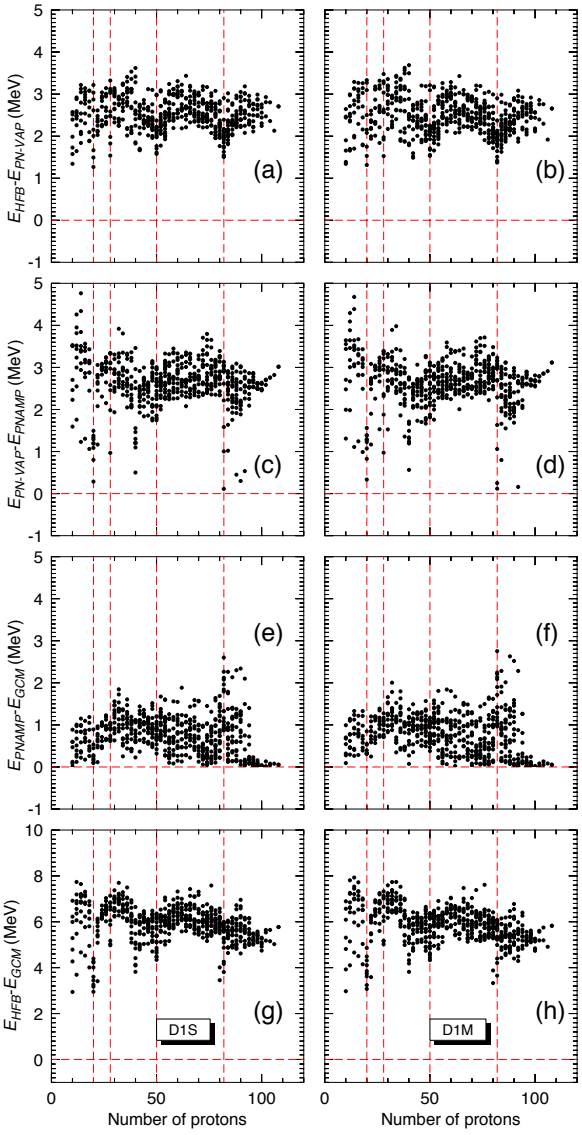

FIG. 7. Same as Fig. 6 but as a function of the number of protons. Dashed vertical lines represent the proton magic numbers 20, 28, 50 and 82.

Since both PNAMP and GCM methods depend crucially on the intrinsic deformation, we also represent the correlation energy gains obtained for the different approaches as a function of the quadrupole deformation β_2 obtained at the HFB level for each nucleus (Fig. 8). In all cases, the largest spread in correlation energy gain is obtained in the spherical point $\beta_2 = 0$. Hence, for this intrinsic deformation we observe energy gains ranging from 1.2-3.5 MeV, 0.0-3.7 MeV and 0.0-2.8 MeV for PN-VAP (Fig. 8(a)-(b)), PNAMP (Fig. 8(c)-(d)), and GCM (Fig. 8(e)-(f)), respectively. These spreads are smaller for

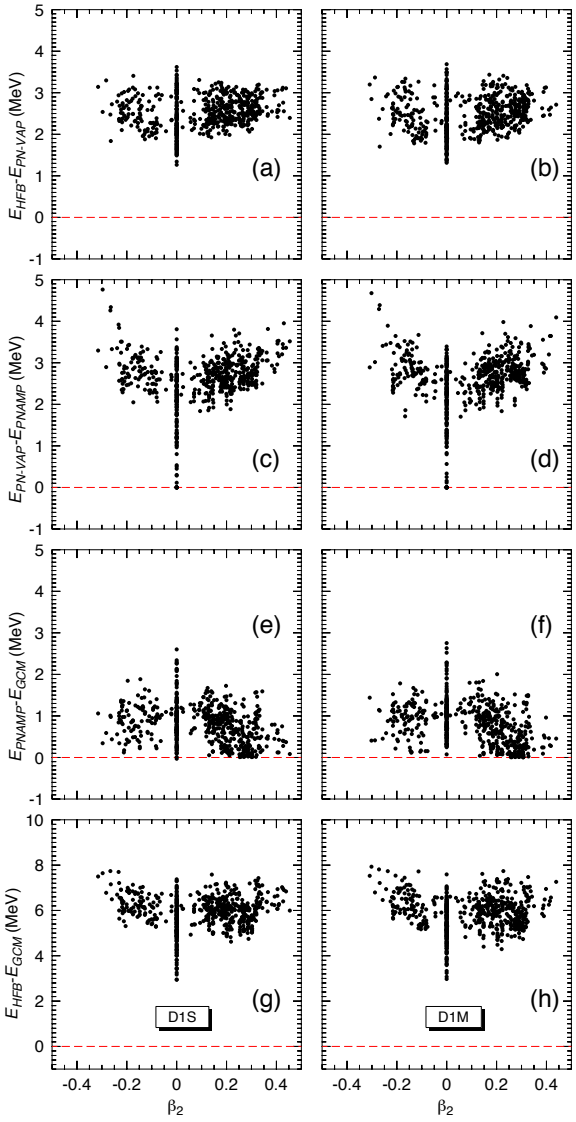

FIG. 8. Same as Fig. 6 but as a function of the quadrupole deformation found at the mean field -HFB- level.

the rest of deformations. Additionally, the energy gain does not depend very much on the size and sign of the quadrupole deformation both in the PN-VAP (Fig. 8(a)-(b)) and GCM (Fig. 8(e)-(f)) approaches. For PNAMP case (Fig. 8(c)-(d)), a mild trend of having larger energy gains with increasing $|\beta_2|$-values is obtained. Similar results are obtained with Skyrme functionals (see Fig. 7 of Ref [25]) showing that these patterns depend on the method rather than on the choice of the functional.

To end this section, we also compare the total correlation energies obtained with the present axial SCCM calculations with those provided by the 5DCH for Gogny D1S given in the supplemental material of Ref. [27]. We observe in Fig. 9 that, except for a few light nuclei, the correlations given by the present method are about $2-3$ MeV larger than the 5DCH ones. Even larger differences

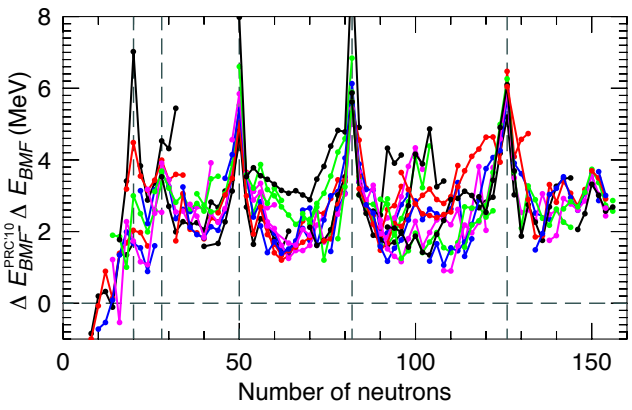

FIG. 9. (color online) Difference between the total correlation energies given by the 5DCH model in Ref. [27] and the ones calculated with the present SCCM method. Isotopic chains are connected by lines with the same color and the interaction in all of the cases is Gogny D1S.

are found around the shell closures since the 5DCH calculation gives positive correlation energies in those nuclei. As a matter of fact, such a anti-correlation energy are set to zero in Ref. [27]. Since the 5DCH method is based on a gaussian overlap approximation, then it is not variationally consistent with the underlying HFB functional. Furthermore, although the triaxial degree of freedom is included in the collective hamiltonian, the present axial SCCM calculations include both symmetry restorations and GCM without GOA that produce larger correlation energies. These SCCM correlation energies are negative everywhere (see Fig. 6(g) for instance) and including other degrees of freedom such as the triaxiality will produce even more negative values. In addition, although convergence of both HFB and SCCM is not globally reached we can at least determine where it has been achieved. Fig. 9 shows that the difference in correlation energies between the present calculations and the 5DCH approach is rather constant along the whole nuclear chart, apart from the spikes around shell closures. This indicates that the 5DCH approach may suffer from similar convergence issues for heavy nuclei. However, one should keep in mind that due to its non-variational nature one cannot strictly speak of converged 5DCH calculations.

B. Comparison with experimental data

1. *Masses*

We now compare the results obtained with the different approximations with the experimental data extracted from the most recent AME [11]. In Fig. 10 the differences between the experimental and theoretical masses are plotted for the different mean field and beyond mean

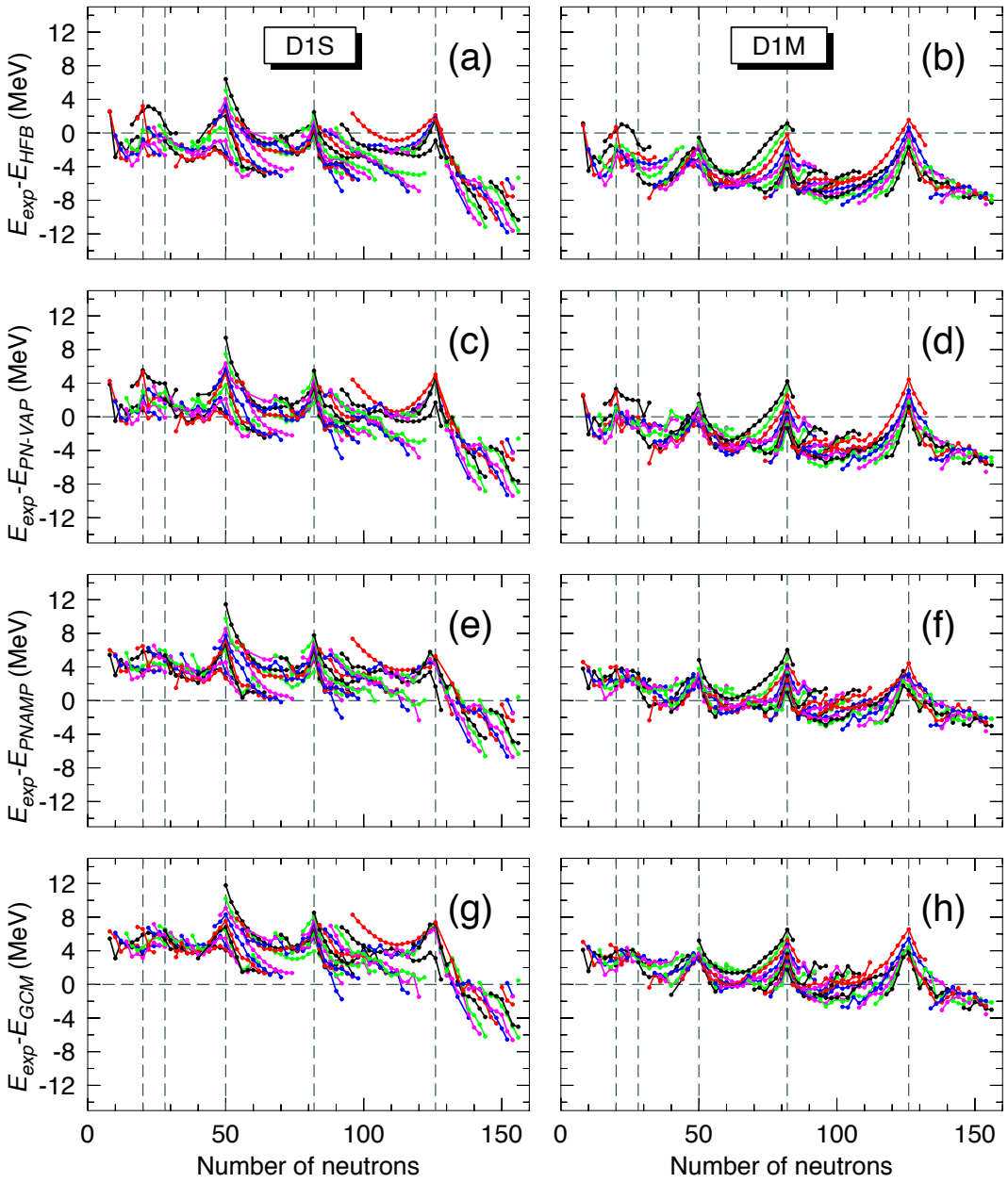

FIG. 10. (color online) Difference between the experimental total energies (taken from Ref. [11]) and: (a)-(b) HFB; (c)-(d) PN-VAP; (e)-(f) PNAMP; (g)-(h) GCM total energies calculated with the Gogny D1S (left panel) and D1M (right panel) parametrizations. Lines connect isotopic chains starting from $Z = 10$. Black, red, blue, magenta and green lines represent isotopic chains with $Z = x0, x2, x4, x6$ and $x8$, being $x = 1, 2, ...$, etc. Dashed vertical lines mark the neutron magic numbers 20, 28, 50, 82 and 126.

field approaches. More quantitative results are written in Table II for the D1S and D1M parametrizations.

Starting from the oldest parametrization, i.e., D1S, we notice first its poor performance in describing experimental masses. In none of the many-body approaches studied here, the root mean square (RMS) deviation is less than 2.6 MeV. This is explained by three major drawbacks of this parametrization (see left panel of Fig. 10). The first one is the presence of residual shell effects. In all of the approaches, peaks at the neutron magic numbers $N = 50$, 82 and 126 are observed. As it was discussed above, BMF energy gains are smaller in the shell closure nuclei (see Fig. 6(g)). Therefore, these peaks are reduced when BMF effects are taken into account but the reduction is clearly insufficient to bring the theory closer to the experiment. The second drawback is the systematic drift towards less bound systems in nuclei with increasing neutron excess. The origin of the

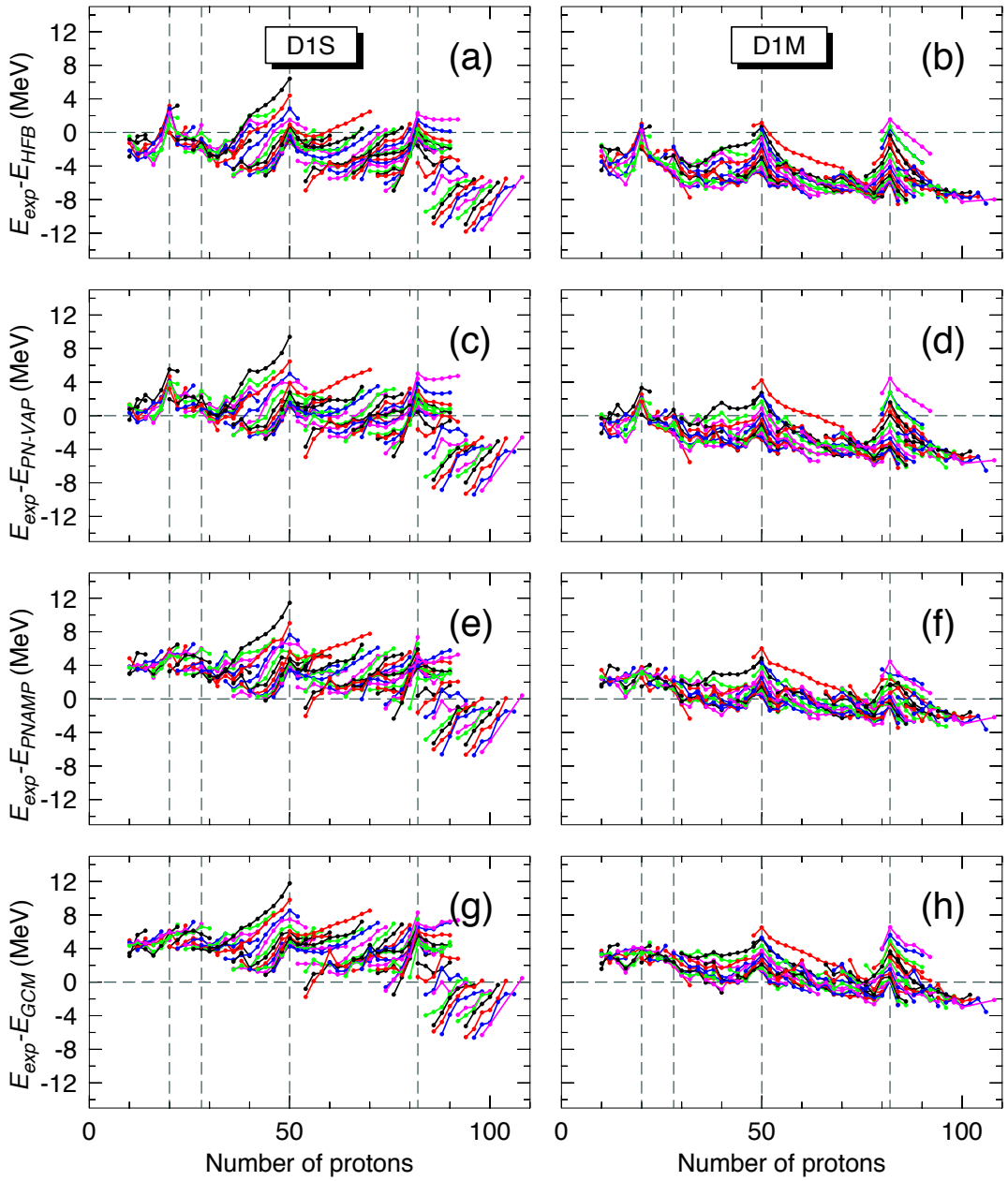

FIG. 11. (color online) Same as Fig. 10 but as a function of the number of protons. Lines connect isotonic chains starting from $N = 10$. Black, red, blue, magenta and green lines represent isotopic chains with $N = x0, x2, x4, x6$ and $x8$, being $x = 1, 2, ...,$ etc. Dashed vertical lines mark the neutron magic numbers 20, 28, 50 and 82.

problem is in the symmetry energy provided by Gogny D1S. This parametrization does not reproduce the correct curvature in the neutron matter equation of state given by *ab-initio* approaches [22] producing a lack of binding energy in neutron rich nuclei. Again, BMF effects do not change this trend. Nevertheless, the spread in light nuclei (from $N = 10 - 40$) found at the mean field and PN-VAP approximations (Fig. 10(a)) is significantly reduced when PNAMP and GCM are taken into account (Figs. 10(e)-(g)). The third drawback is the way in which the parameters of the interaction were obtained. Hence, the parameters of the oldest realizations of the Gogny interaction were fitted to reproduce experimental data with the HFB method but leaving some room for eventual beyond-mean-field effects [45]. However, some overbinding is still obtained with respect to the experimental values. The evolution of the RMS values given in the second column of Tab. II reflects also this effect, obtaining for the most sophisticated many-body method used in this work a RMS deviation of 4.45 MeV (for 598

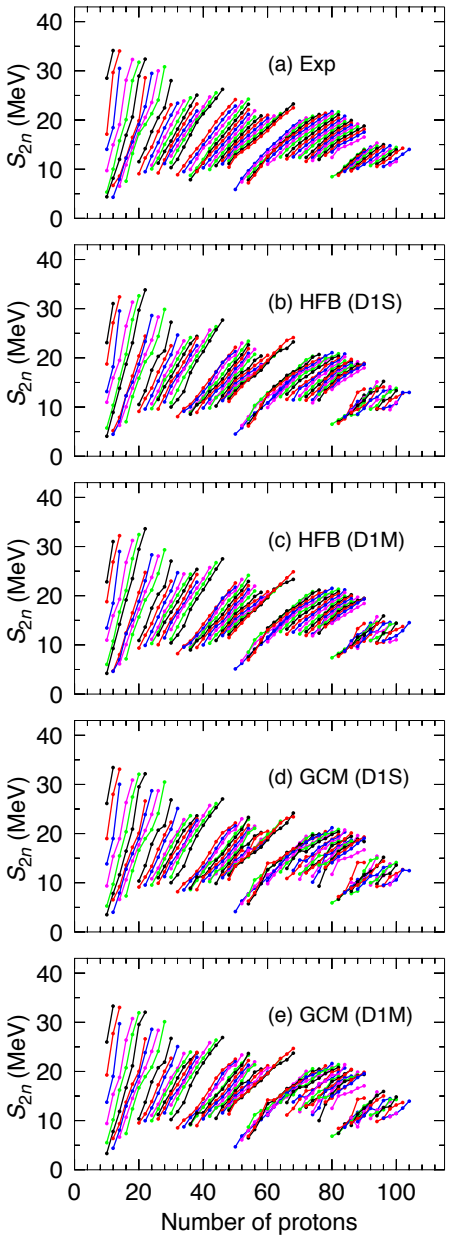

FIG. 12. (color online) Two-neutron separation energies as a function of the number of protons: (a) Experimental data (taken from Ref. [11]); (b) HFB; (d) GCM calculated with the Gogny D1S parametrization and (c) HFB ; (e) GCM calculated with D1M parametrization. Lines connect isotonic chains starting from $N = 10$. Black, red, blue, magenta and green lines represent isotopic chains with $N = x0, x2, x4, x6$ and $x8$, being $x = 1, 2, ...,$ etc.

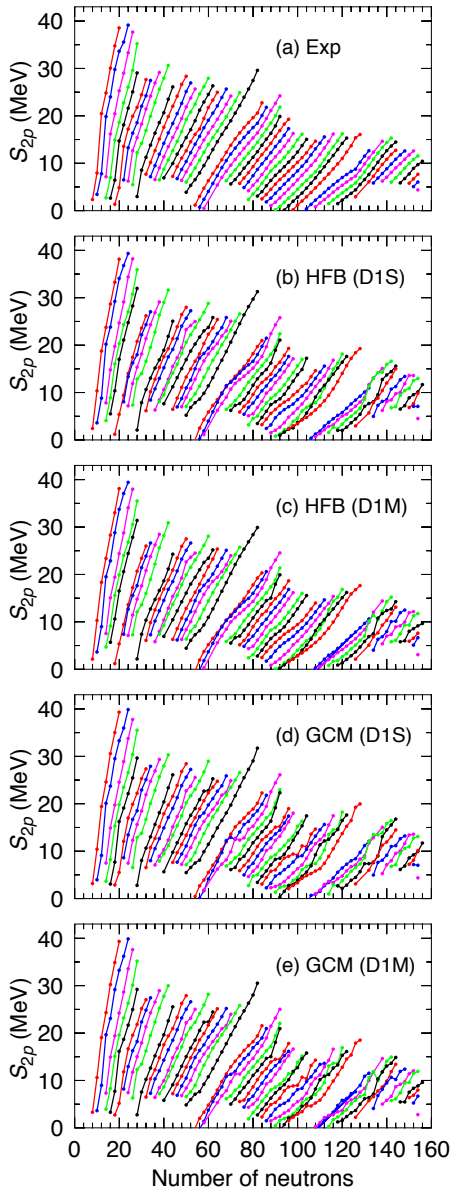

FIG. 13. (color online) Two-proton separation energies as a function of the number of neutrons: (a) Experimental data (taken from Ref. [11]); (b) HFB; (c) GCM calculated with the Gogny D1S parametrization. Lines connect isotopic chains starting from $Z = 12$. Black, red, blue, magenta and green lines represent isotopic chains with $Z = x0, x2, x4, x6$ and $x8$, being $x = 1, 2, ...,$ etc...

masses).

The D1M parametrization [9] was built to correct these shortcomings of the D1S by performing a fit to a large set of experimental masses using the 5DCH method [27] to include beyond-mean-field effects. That led to a RMS deviation from data of ~ 0.798 MeV (for 2149 masses). Except for the inclusion of triaxiality and the lack of quantum number projections, the 5DCH method can be considered as a gaussian overlap approximation (GOA) of the method used in this work [35]. Let us analyze now the performance of D1M in combination with the present axial SCCM method which does not assume such a GOA approximation. In the right panel of Fig. 10 the difference between experimental and theoretical masses obtained with the D1M parametrization are shown. Here we observe that the drift and, partially, the overbinding found

with the D1S parametrization are corrected. However, as it was already stated in Ref. [9], strong shell effects are still present and the theoretical results that overestimate the binding energies around the magic neutron numbers, particularly at $N = 50$, 82 and 126. This behavior is not corrected by including BMF correlations of the kind studied in this work. Nevertheless, the addition of correlations improves the agreement with data with respect to the mean field results. Since the D1M parameters were fitted taking already into account BMF effects, the results at the HFB level are underbound with respect to the experimental values (Fig. 10(b)). A very large RMS deviation is obtained for this approach and a much smaller for the rest (see Table II). However, the correlation energies attained by the GCM are larger than the ones provided by the 5DCH, as discussed above. This produces an excess of total energy also with this parametrization when the axial shape mixing with quantum number projection is taken into account (Fig. 10(h)). The RMS value for the GCM approach with the D1M parametrization is 2.17 (for 598 masses).

It is worth mentioning that the global RMS values themselves do not provide the complete picture of the comparison with the experimental data since some compensation effects can occur in different regions of the nuclear chart. A RMS-value independent on the number of particles -including BMF effects- must be pursued even though an excess of total energy would be expected when BMF corrections are incorporated on top of a functional fitted to reproduce data with less correlated ground states. In this sense, BMF corrections work better in reducing the spread and shell gaps in $N \leq 28$ nuclei than in heavier systems (see Fig. 10) although, from the point of view of the RMS, light nuclei are farther away from the experiment than the heavy ones.

TABLE II. RMS comparison between theoretical calculations and experimental data for total energies, two neutron and two proton separation energies. All energies are in MeV.

D1S	E	S_{2n}	S_{2p}
HFB	3.53	0.98	1.15
PN-VAP	2.62	1.10	1.11
PNAMP	3.75	0.98	1.00
GCM	4.45	0.95	1.00
D1M	E	S_{2n}	S_{2p}
HFB	5.29	0.89	0.99
PN-VAP	3.14	1.03	0.96
PNAMP	1.79	0.89	0.86
GCM	2.17	0.85	0.87

In order to check the possible shells effects appearing in isotonic chains, we represent in Fig. 11 the energy differences with the experimental masses obtained for the different many-body approaches and parametrizations as a function of the number of protons. These shell effects, though still present, are slightly less pronounced than in the isotopic chains. This is in agreement with the results found with Skyrme interactions [25]. However, it is interesting to note that the relative overbinding found at $Z = 20$ at the HFB level is smoothened out with BMF approaches in both parametrizations while $Z = 50$ and 82 persist. Finally, we observe a clear difference between the results provided by the two parametrizations. For D1M rather symmetric energy differences around the shell closures are found while for D1S larger energies are obtained for larger values of Z within a given isotonic chain. Since the isotonic chains start normally with $N > Z$, this behavior reflects again a lack of ground state energy provided by the D1S parametrization in nuclei with neutron excess, i.e., the symmetry energy problem already mentioned.

TABLE III. Logarithmic errors and deviations for the 2_1^+ excitation energies computed for GCM-D1S, GCM-D1M, GCM-SLy4 [63] and 5DCH-D1S [27, 64]. Experimental data are taken from Ref. [62].

	GCM-D1S (534)	GCM-D1M (534)	GCM-SLy4 (359)	5DCH-D1S (513)	5DCH-D1S (519)
$\bar{R}_E$	0.32	0.35	0.51	0.11	0.12
σ_E	0.42	0.43	0.38	0.35	0.33

To conclude this section, we can state that both the symmetry energy problem and the overbinding produced by the inclusion of BMF effects can be solved by modifying the parametrization, as it is almost done with the introduction of the Gogny D1M interaction. However, the energy excess obtained in the magic nuclei (relative to the energy predicted in the mid-shell nuclei), although reduced, is not washed out by taking into account the present BMF effects. It is still an open question whether the current BMF functionals, with parameters self-consistently fitted and probably extended to include other collective degrees of freedom and symmetry restorations, are able to produce flat energy differences instead of the parabolic behavior found in Figs. 10-11 (and in Refs. [9, 22, 25, 27]). These tasks are highly demanding, both the refit of the interaction and the inclusion of, for example, pairing fluctuations [54], triaxial [38, 55–57] and/or octupole [58, 59] shapes with the corresponding symmetry restorations and configuration mixing. On the other hand, it is possible that the central, spin-orbit and density-dependent terms of the starting Gogny interaction have to be modified including, for instance, explicit tensor terms [60, 61].

Finally, since the present calculations are not fully converged, neither other degrees of freedom are taken into account -triaxiality, octupolarity, etc.- RMS values for D1S and/or D1M parametrizations given in Table II should be considered as a qualitative description of the effect on the masses produced by the different approaches rather than the final values.

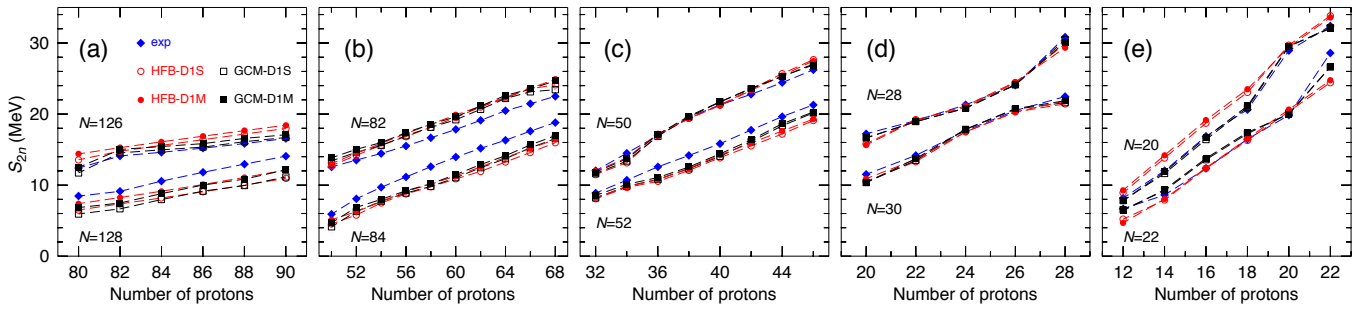

FIG. 14. (color online) Two-neutron separation energies for (a) $N = 126, 128$; (b) $N = 82, 84$; (c) $N = 50, 52$; (d) $N = 28, 30$; and (e) $N = 20, 22$ isotonic chains. Blue diamonds, red circles and black boxes represent the experimental, mean field and GCM results respectively. Empty (full) symbols are calculated with the Gogny D1S (D1M) parametrization.

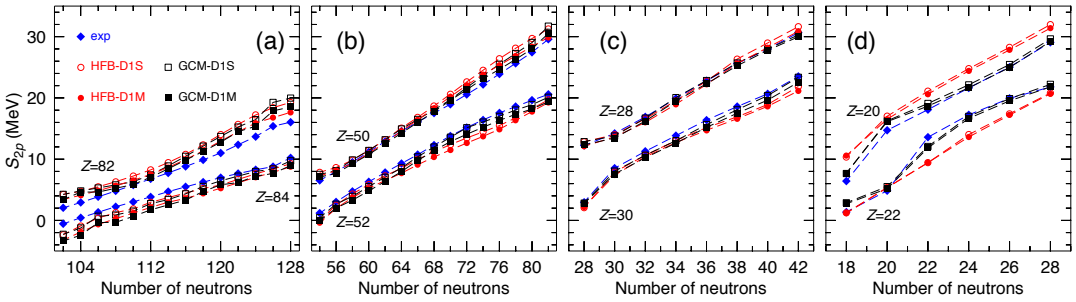

FIG. 15. (color online) Two-proton separation energies for (a) $Z = 82, 84$; (b) $Z = 50, 52$; (c) $Z = 28, 30$; and (d) $N = 20, 22$ isotopic chains. Blue diamonds, red circles and black boxes represent the experimental, mean field and GCM results respectively. Empty (full) symbols are calculated with the Gogny D1S (D1M) parametrization.

2. *Two particle separation energies and shell gaps*

Most of the times, the relevant quantities for calculating reaction rates, Q-values, etc., with astrophysical interest are not the absolute energies shown in the previous section but energy differences between those masses. We analyze now its performance on two-nucleon separation energies (S_{2n}, S_{2p}), since the present GCM method with the Gogny functional is not well developed for computing odd-nuclei yet:

$$S_{2n}(Z,N) = E(Z,N-2) - E(Z,N)$$
$$S_{2p}(Z,N) = E(Z-2,N) - E(Z,N) \qquad (15)$$

These quantities are plotted in Figs. 12- 13 and analyzed quantitatively in Table II. The overall behavior of the experimental values is quite well reproduced. The RMS deviations from experimental values for S_{2n} and S_{2p} are much better than in the masses for both parametrizations. However, we observe important local differences between the experimental data and theory. On the one hand, the experimental curves are much smoother, having always for a constant number of protons (neutrons) a continuous decrease in the S_{2n} (S_{2p}) when adding neutrons (protons). This is not the case for the theoretical data, where jumps and crossings between isotonic (isotopic) chains in the S_{2n} (S_{2p}) separation energies are shown. This drawback is obtained all over the nuclear chart independently on the parametrization and is a bit larger in the GCM approach than in the HFB result. Its origin could be related to a convergence problem discussed in Sec. II and/or the lack of other degrees of freedom such as triaxiality or octupolarity.

Finally, we analyze the neutron and proton shell gaps associated to magic numbers by zooming in the S_{2n} energies for N = 20, 22, 28, 30, 50, 52, 82, 84, 126, 128 isotonic chains and the S_{2p} energies for Z = 20, 22, 28, 30, 50, 52, 82, 84 isotopic chains in Figs. 14-15. We observe first that the different parametrizations (D1S and D1M) provide for this set of nuclei very similar results. Furthermore, the mean field approach tend to predict larger shell gaps than the experimental ones except for $N, Z = 28$ magic numbers, where the agreement with the experimental data is very good. Correlations beyond the static mean field tend to reduce these gaps, almost matching the experimental results in $N, Z = 20$ and $Z = 50$. However, the reduction is not enough to reproduce the actual gaps in $N = 50$, 82, 126 nor $Z = 82$. Therefore, the shell quenching obtained by including BMF effects reported by Bender et al. in Ref. [26] and by Delaroche et al. in Ref. [27] is only partially re-

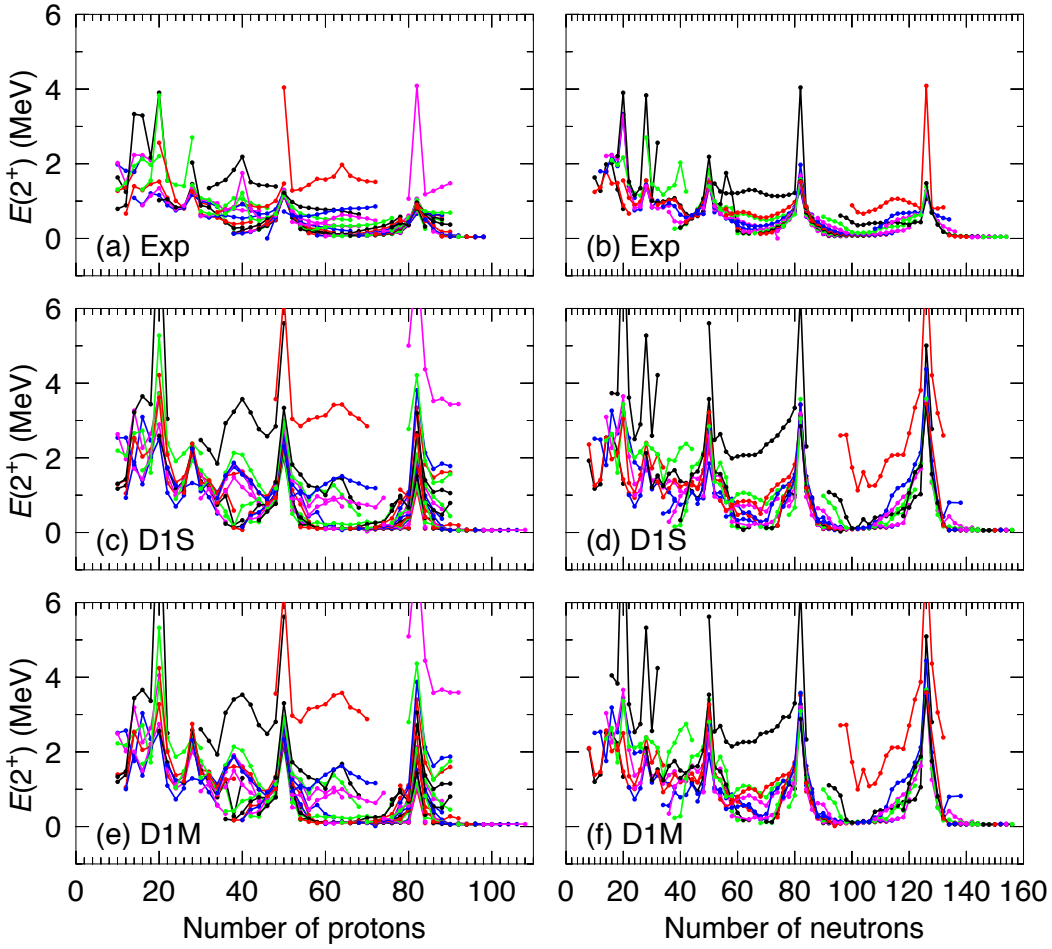

FIG. 16. (color online) 2_1^+ excitation energies for: (a)-(b) Experimental data (taken from Ref. [62]); (c)-(d) GCM-Gogny D1S; and (e)-(f) GCM-Gogny D1M. Lines connect isotonic chains starting from $N = 10$ (left panel) and isotopic chains starting from $Z = 10$ (right panels). The color code is the same as in previous figures.

produced here. In addition, the latter results are much smoother than the results shown in Figs. 12-13. As it was mentioned above (see Fig. 9), the amount of BMF correlation energies obtained by the present SCCM method is larger than the one obtained by solving the 5DCH model, even though in the latter the triaxiality is included. Furthermore, calculations reported in Refs. [25, 26] are very similar to the ones presented here except for the use of GOA (and topGOA) approximations. Therefore, the smoothness of the S_{2n} (S_{2p}) separation energies in such calculations could be related to the GOA approximations used in those references. Nevertheless, a better convergence and the addition of other degrees of freedom are needed to check whether the present interactions can reproduce the smoothness of the experimental data.

3. 2_1^+ excitation energies

We finally compare the 2_1^+ excitation energies obtained with our present GCM global calculations with the experimental data compiled in Ref. [62]. It is important to note again that the convergence of the results are not fully guaranteed, especially in heavy nuclei where a working basis including eleven major oscillator shells could be too small (see Sec. II and Fig.5, bottom panel). Therefore, the values obtained with this reduced space must be taken with caution. In any case, we consider these results relevant to extract a global performance of the method, and, in particular, to compare the results provided by the two Gogny parametrizations for this observable. We can also compare with the results of similar studies already reported with the Skyrme SLy4 [63] (with a topological gaussian overlap approximation in the angular momentum projection and a limited number of intrinsic states in the GCM) and Gogny D1S [27, 64] within the 5DCH

framework. However, in the latter cases an educated selection of nuclei where the method is better suited was made and sets of 359 [63], 519 [64] and 513 [27] nuclei were chosen in these papers.

Both the experimental values and the results of the GCM calculations for the 2_1^+ energies are shown in Fig. 16. We observe clearly an enhancement of the excitation energies at the proton and neutron magic numbers. Additionally, the 2_1^+ excitation energies corresponding to $N = 20$, 28, 50, 82 and 126 isotonic chains and Ca, Ni, Sn and Pb isotopes are clearly above the rest both experimentally and in the calculations. On the other hand, we see that the two parametrizations provide almost identical results for this observable even though they behave very different for masses. The global behavior of the experimental data is well reproduced although the calculations show a less smooth behavior and a systematic overestimation of the experimental values.

The latter drawback can be better seen in Fig. 17(a)-(b), where the theoretical values versus the experimental energies are represented for D1S and D1M parametrizations respectively. Although we observe a clear correlation between the two quantities, the theoretical predictions tend to overestimate the empirical values. We do not find significant differences between the D1S and D1M parametrizations. To better estimate quantitatively the differences with the experimental results we follow the analysis performed in Refs. [27, 63, 64]. In these works, the so-called logarithmic error -R_E- and its standard deviation -σ_E- from the average -$\bar{R}_E$- are defined as:

$$R_E = \log\left[E(2_1^+)_{\rm th}/E(2_1^+)_{\rm exp}\right] \tag{16}$$

$$\sigma_E = \langle\left(R_E - \bar{R}_E\right)^2\rangle^{1/2} \tag{17}$$

In Fig. 17(c)-(d) we show histograms representing the number of nuclei with a given value of R_E for D1S and D1M parametrizations. We find rather symmetric distributions with mean values and standard deviations of $\bar{R}_E = 0.32(0.35)$ and $\sigma_E = 0.42(0.43)$ respectively for D1S (D1M). Similar results are obtained with Skyrme SLy4 [63] with a more restricted set of nuclei (see Table III). This systematic drift towards larger values is a consequence of the variational method. In this framework, the ground state 0_1^+ are favored with respect to other states, pulling down its energy and stretching the final spectra. The inclusion of additional degrees of freedom such as triaxiality, time-reversal symmetry breaking and quasiparticle excitations, which are more relevant in the excited states than in the ground state, allows a variational description of these excited states and the excitation energies can be reduced. For example, local studies with a GCM method including triaxial angular momentum projection [38, 55–57] or pairing fluctuations [54] have already shown this effect. On the other hand, quantum number projections and GCM can modify significantly both the equilibrium deformation of the system (^{32}Mg is the paradigm for this effect [37]) and the collective masses. Since these parametrizations are not fitted with using the BMF many-body states of this work, the MF and BMF collective behavior can be different. For instance, angular momentum projection could overestimate a quadrupole deformation that could be correct at the HFB level. Therefore, the excitation energies should be taken into account in a future refit of the interaction.

We finally comment on the smaller deviation and dispersion obtained with Gogny D1S using the 5DCH method [27] shown in Table III. In this case, the inclusion of the triaxial degree of freedom and the fit of the inertia parameters with a cranking approximation can improve the description of the 2_1^+ excitation energies. However, since 5DCH does not include either particle number or angular momentum projection, spurious contributions of MF states with the wrong quantum numbers can produce a collapse of the excited states [54]. In any case, further analyses, beyond the scope of this work, are needed to compare the 5DCH approach with a full SCCM approximation.

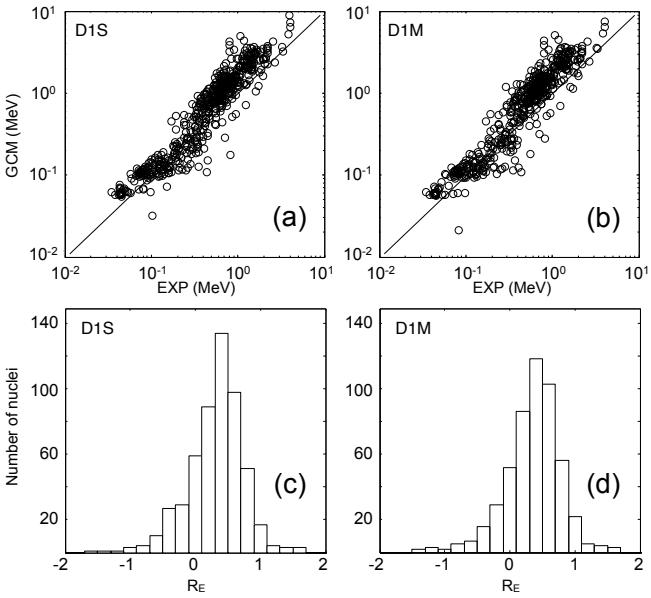

FIG. 17. GCM versus experimental 2_1^+ excitation energies for (a) D1S and (b) D1M parametrizations. (c)-(d) Histograms of the logarithmic errors of the 2_1^+ states.

IV. SUMMARY AND OUTLOOK

In this work, correlation energies, total energies, two neutron separation energies and 2_1^+ excitation energies for a large set of even-even nuclei along the nuclear chart have been presented. The theoretical results have been obtained by using self-consistent mean field (HFB) and beyond-mean-field (BMF) methods, including particle number and angular momentum restorations and axial quadrupole shape mixing without gaussian overlap approximations. The underlying interaction used

in all of the calculations was Gogny with two different parametrizations, D1S and D1M. The convergence of the results as a function of the number of harmonic oscillator shells included in the basis has been analyzed. Hence, the convergence of the total energies are not fully guaranteed and extrapolation schemes to infinite bases should be implemented in the near future. Nevertheless, a large number of harmonic oscillator shells, $N_{s.h.o.} = 19$, has been used for the HFB part, showing a better performance than the usual rule of having a number of single particle states equal to eight times the larger number among the protons and neutrons of a given nucleus. Additionally, the calculated BMF correlations and particle separation energies are less dependent on the number of harmonic oscillator shells than the total energies. Concerning those BMF correlations, both parametrizations, D1S and D1M, give similar correlation energies with respect to their mean field solutions.

Compared to the experimental data, the D1S parametrization shows a symmetry energy problem which produces a lack of binding energy in neutron rich systems. This fact is reflected in a drift in the difference between theoretical and experimental energies for nuclei with a neutron excess which is corrected in the D1M parametrization. However, strong shell effects (stronger as a function of the neutron number) are still present in both realizations and parabolic instead of flat energy differences are found between two consecutive magic numbers. BFM correlations tend to reduce these differences since rotational and vibrational corrections are larger in the mid-shell than in closed shell nuclei, but this reduction is not sufficient to remove the difference between the experimental and theoretical values.

Energy differences such as two-neutron separation energies are in a better agreement with experimental data but still not satisfactory. Hence, BMF correlations bring the theoretical predictions towards the experimental values for $N, Z = 20$ shell gaps. However, some problems like artificial jumps, crossing and overestimation of the shell gaps for heavier are found in the calculations and they are not fully corrected by including BMF effects.

Additionally, we have reported the results for 2_1^+ excitation energies calculated with $N_{s.h.o.} = 11$ shells. We have obtained similar results for D1S and D1M parametrizations, having a systematic stretching of the 2_1^+ energies which is more related to the method used to solve the many-body problem rather than the parametrization itself.

As an outlook, some improvements should be taken into account in the near future, in particular:

1. Convergence of the results with the properties of the harmonic oscillator working basis.

2. Triaxial and other degrees of freedom should be included explicitly in the calculations.

In the long-term, a new parametrization of the Gogny interaction (or any other type of energy density functional) including in the fitting procedure fully converged SCCM corrections with triaxial and octupolar states is desirable.

Finally, new experimental data would be very helpful to constrain further the current and future models.

ACKNOWLEDGEMENTS

We acknowledge the support from GSI-Darmstadt and CSC-Loewe-Frankfurt computing facilities. This work was supported by the BMBF-Verbundforschungsprojekt number 06DA7047I, the Ministerio de Economía y Competitividad-Programa Ramón y Cajal 2012 number 11420 and the Helmholtz Association through the Nuclear Astrophysics Virtual Institute (VH-VI-417).

[1] K. Blaum, Phys. Repts. 425, 1 (2006).
[2] P. Möller, J. R. Nix, W. D. Myers, and W. J. Swiatecki, At. Data Nucl. Data Tables 59, 185 (1995).
[3] P. Möller, W. D. Myers, H. Sagawa, and S. Yoshida, Phys. Rev. Lett. 108, 052501 (2012).
[4] N. Wang, M. Liu, and X. Wu, Phys. Rev. C 81, 044322 (2010).
[5] N. Wang, M. Liu, X. Wu, J. Meng, Phys. Lett. B 734, 215 (2014).
[6] J. Duflo and A. P. Zuker, Phys. Rev. C 52, R23 (1995).
[7] S. Goriely, N. Chamel, and J. M. Pearson, Phys. Rev. C 88, 024308 (2013).
[8] S. Goriely, N. Chamel, and J. M. Pearson, Phys. Rev. C 88, 061302(R) (2013).
[9] S. Goriely, S. Hilaire, M. Girod, and S. Péru, Phys. Rev. Lett. 102, 242501 (2009).
[10] A. H. Wapstra, G. Audi and C. Thibault, Nucl. Phys. A 729, 129 (2003).
[11] M. Wang, G. Audi, A. H. Wapstra, F.G. Kondev, M. MacCormick, X. Xu, and B. Pfeiffer, Chinese Phys. C 36, 1603 (2012).
[12] A. Arcones and G. Martínez-Pinedo, Phys. Rev. C 83, 045809 (2011).
[13] S. Brett, I. Bentley, N. Paul, R. Surman, and A. Aprahamian, Eur. Phys. J. A 48, 184 (2012).
[14] R. Roth, J. Langhammer, A. Calci, S. Binder, and P. Navratil, Phys. Rev. Lett. 107, 072501 (2011).
[15] D. J. Dean and M. Hjorth-Jensen, Phys. Rev. C 69, 054320 (2004).
[16] H. Hergert, S. Binder, A. Calci, J. Langhammer, and R. Roth, Phys. Rev. Lett. 110, 242501 (2013).
[17] V. Soma, C. Barbieri, and T. Duguet, Phys. Rev. C 87, 011303 (2013).
[18] T. Otsuka, T. Suzuki, J. D. Holt, A. Schwenk, and Y. Akaishi, Phys. Rev. Lett. 105, 032501 (2010).
[19] D. Steppenbeck, S. Takeuchi, N. Aoi, P. Doornenbal, M. Matsushita, H. Wang, H. Baba, N. Fukuda, S. Go,

M. Honma, J. Lee, K. Matsui, S. Michimasa, T. Motobayashi, D. Nishimura, T. Otsuka, H. Sakurai, Y. Shiga, P.-A. Söderström, T. Sumikama, H. Suzuki, R. Taniuchi, Y. Utsuno, J. J. Valiente-Dobón, and K. Yoneda Nature 502, 207 (2013).
[20] J. D. Holt, J. Menéndez, and A. Schwenk, Phys. Rev. Lett. 110, 022502 (2013).
[21] N. Chamel, S. Goriely, and J.M. Pearson, Nucl. Phys. A 812, 72 (2008).
[22] F. Chappert, M. Girod, and S. Hilaire, Phys. Lett. B 668, 420 (2008).
[23] S. Goriely, M. Samyn, and J. M. Pearson, Phys. Rev. C 75, 064312 (2007).
[24] M. Bender, P.-H. Heenen, and P.-G. Reinhard, Rev. Mod. Phys. 75, 121 (2003).
[25] M. Bender, G. F. Bertsch, and P.-H. Heenen, Phys. Rev. C 73, 034322 (2006).
[26] M. Bender, G. F. Bertsch, and P.-H. Heenen, Phys. Rev. C 78, 054312 (2008).
[27] J.-P. Delaroche, M. Girod, J. Libert, H. Goutte, S. Hilaire, S. Péru, N. Pillet, and G. F. Bertsch, Phys. Rev. C 81, 014303 (2010).
[28] K. Q. Lu, Z. X. Li, Z. P. Li, J. M. Yao, and J. Meng, Phys. Rev. C 91, 027304 (2015).
[29] J.-F. Berger, M. Girod, and D. Gogny, Nucl. Phys. A428, 23c (1984).
[30] J.-F. Berger, M. Girod, and D. Gogny, Comput. Phys. Commun. 63, 365 (1991).
[31] B. Bally, B. Avez, M. Bender, and P.-H. Heenen, Phys. Rev. Lett. 113, 162501 (2014).
[32] P. Möller, R. Bengtsson, B. G. Carlsson, P. Olivius, and T. Ichikawa, Phys. Rev. Lett. 97, 162502 (2006).
[33] L. M. Robledo and G. F. Bertsch, Phys. Rev. C 84, 054302 (2011).
[34] L. M. Robledo, J. Phys. G: Nucl. Part. Phys. 42, 055109 (2015).
[35] P. Ring, and P. Schuck, *The nuclear many-body problem*, Springer-Verlag, Berlin, 1980.
[36] D. Lacroix, T. Duguet, and M. Bender, Phys. Rev. C 79, 044318 (2009).
[37] R. Rodríguez-Guzmán, J. L. Egido, and L. M. Robledo, Nucl. Phys. A 709, 201 (2002).
[38] T. R. Rodríguez, J. L. Egido, Phys. Rev. C 81, 064323 (2010).
[39] Although the working basis is spherical, the HFB states, defined by the transformation given in Eq. 3, can be deformed.
[40] M. Anguiano, J. L. Egido, and L. M. Robledo, Nucl. Phys. A696, 467 (2001).
[41] L. M. Robledo, HFBAXIAL code, Universidad Autónoma de Madrid (2002).
[42] T. R. Rodríguez, J. L. Egido, Phys. Rev. Lett. 99, 062501 (2007).
[43] https://wiki.gsi.de/cgi-bin/view/Linux/GridEngine
[44] http://csc.uni-frankfurt.de/index.php?id=51&L=0
[45] J. Dechargé and D. Gogny, Phys. Rev. C 21, 1568 (1980).
[46] J. Decharge, L. Sips, Nucl. Phys. A 407, 1 (1983).
[47] S. Hilaire, and M. Girod, Eur. Phys. J. A, 33, 237 (2007).
[48] R. J. Furnstahl, G. Hagen, and T. Papenbrock, Phys. Rev. C 86, 031301 (2012).
[49] S. N. More, A. Ekström, R. J. Furnstahl, G. Hagen, and T. Papenbrock, Phys. Rev. C 87, 044326 (2013).
[50] R. J. Furnstahl, S. N. More, and T. Papenbrock, Phys. Rev. C 89, 044301 (2014).
[51] S. König, S. K. Bogner, R. J. Furnstahl, S. N. More, and T. Papenbrock, Phys. Rev. C 90, 064007 (2014).
[52] A. Arzhanov, T. R. Rodríguez, G. Martínez-Pinedo, in preparation.
[53] J. E. García-Ramos and K. Heyde, Phys. Rev. C 89 014306 (2014).
[54] N. L. Vaquero, J. L. Egido, and T. R. Rodríguez, Phys. Rev. C 88, 064311 (2013).
[55] M. Bender and P.-H. Heenen, Phys. Rev. C 78, 024309 (2008).
[56] J. M. Yao, J. Meng, P. Ring, and D. Vretenar, Phys. Rev. C 81, 044311 (2010).
[57] T. R. Rodríguez, Phys. Rev. C 90, 034306 (2014).
[58] P. A. Butler and W. Nazarewicz, Rev. Mod. Phys. 68, 349 (1996).
[59] E. Garrote, J. L. Egido, and L. M. Robledo, Phys. Rev. Lett. 80, 4398 (1998).
[60] T. Otsuka, T. Matsuo, and D. Abe, Phys. Rev. Lett. 97, 162501 (2006).
[61] M. Anguiano, M. Grasso, G. Co, V. De Donno, and A. M. Lallena, Phys. Rev. C 86, 054302 (2012).
[62] S. Raman, C. W. Nestor, and P. Tikkanen, At. Data Nucl. Data Tables 78, 1 (2001).
[63] B. Sabbey, M. Bender, G. F. Bertsch, and P.-H. Heenen, Phys. Rev. C 75, 044305 (2007).
[64] G. F. Bertsch, M. Girod, S. Hilaire, J.-P. Delaroche, H. Goutte, and S. Péru, Phys. Rev. Lett. 99, 032502 (2007).